4-26-2022

Selective axonal transport through branch junctions is directed by growth cone signaling and mediated by KIF1/kinesin-3 motors.

Stephen R. Tymanskyj
Thomas Jefferson University

Bridget M. Curran
Thomas Jefferson University

Le Ma
Thomas Jefferson University

Follow this and additional works at: https://jdc.jefferson.edu/department_neuroscience

Part of the Neurosciences Commons
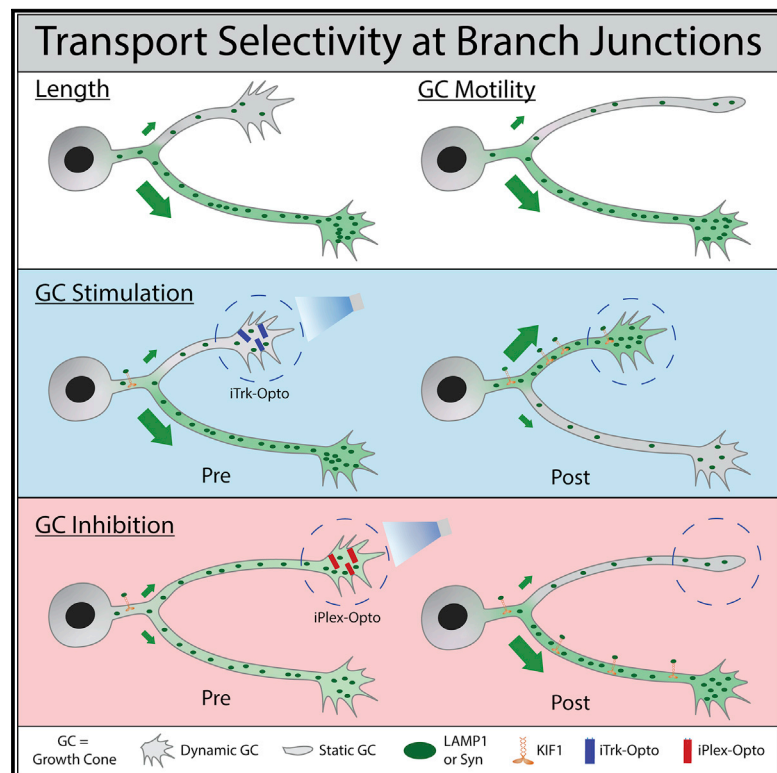
Let us know how access to this document benefits you

Recommended Citation

Cell Reports

Selective axonal transport through branch junctions is directed by growth cone signaling and mediated by KIF1/kinesin-3 motors

Graphical abstract

Authors
Stephen R. Tymanskyj, Bridget M. Curran, Le Ma

Correspondence
le.ma@jefferson.edu

In brief
Tymanskyj et al. report that anterograde transport of LAMP1 and synaptic vesicles through branch junctions is not random but rather favors longer branches or branches with dynamic growth cones. This bias, termed transport selectivity, can be controlled by local activation of growth signaling and depends on KIF1/kinesin-3 motors.

Highlights

- Anterograde axonal transport through branch junctions is not random but selective

- Selectivity is impacted by branch length and more strongly by growth cone motility

- Optogenetic activation of growth cone signaling redirects anterograde transport

- KIF1/kinesin-3 mediates the signal-dependent transport selectivity

CellPress

Cell Reports

Report

Selective axonal transport through branch junctions is directed by growth cone signaling and mediated by KIF1/kinesin-3 motors

Stephen R. Tymanskyj,[1] Bridget M. Curran,[1] and Le Ma[1,2,*]
[1]Department of Neuroscience, Jefferson Center for Synaptic Biology, Vickie and Jack Farber Institute for Neuroscience, Sydney Kimmel Medical College, Thomas Jefferson University, Philadelphia, PA 19107, USA
[2]Lead contact
*Correspondence: le.ma@jefferson.edu
https://doi.org/10.1016/j.celrep.2022.110748

SUMMARY

Development and function of nerve cells rely on the orchestration of microtubule-based transport from the cell body into distal axonal terminals. Neurons often have highly elaborate branches innervating multiple targets, but how protein or membrane cargos navigate through branch junctions to specific branch targets is unknown. Here, we demonstrate that anterograde transport of membrane vesicles through axonal branch junctions is highly selective, which is influenced by branch length and more strongly by growth cone motility. Using an optogenetic tool, we demonstrate that signaling from the growth cone can rapidly direct transport through branch junctions. We further demonstrate that such transport selectivity is differentially regulated for different vesicles and mediated by the KIF1/kinesin-3 family motors. We propose that this transport regulation through branch junctions could broadly impact neuronal development, function, and regeneration.
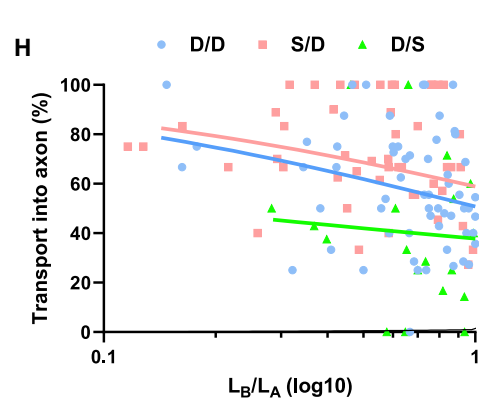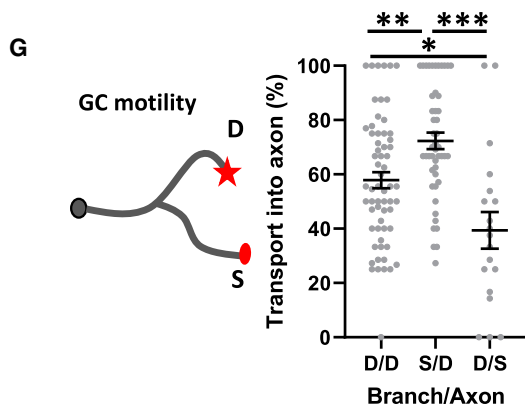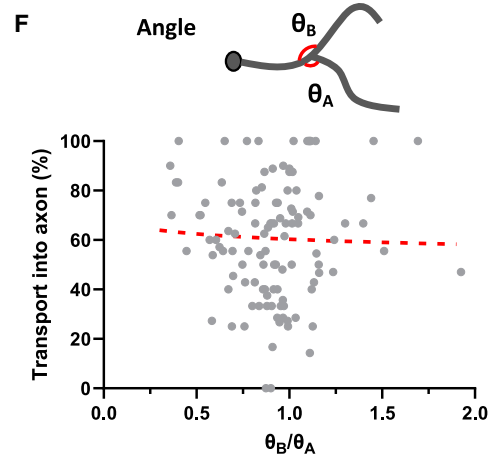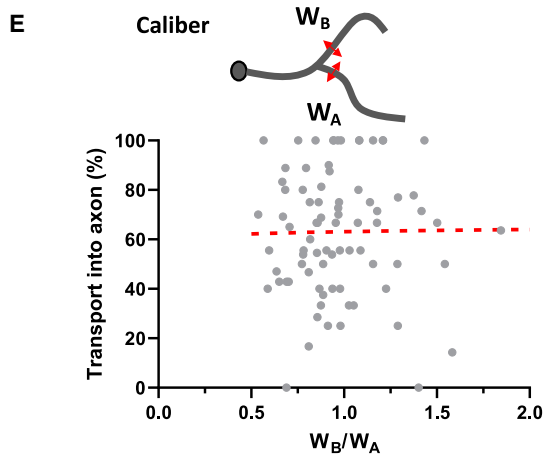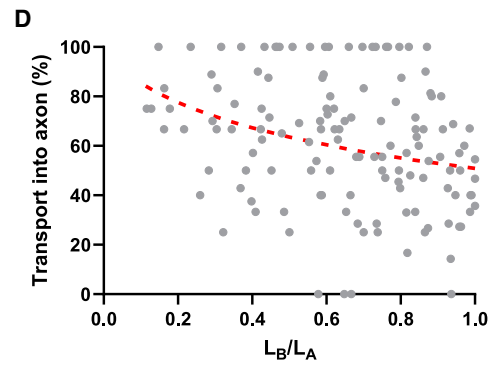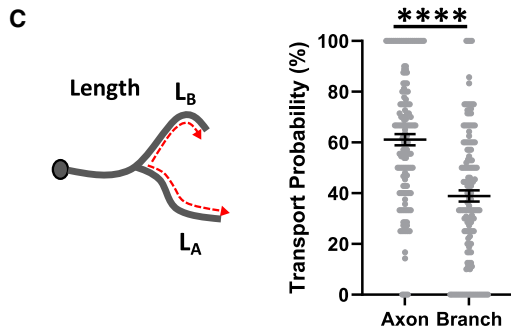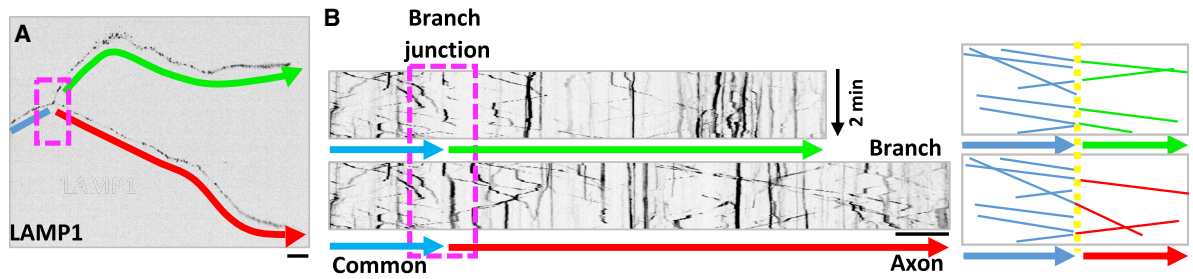
INTRODUCTION

Microtubule-based axonal transport is fundamental to multiple processes throughout the life of a neuron, encapsulating circuit formation, neuronal maintenance, and synaptic plasticity. It is powered by molecular motors that move protein or membrane cargos formed in the cell body to distal terminals along axonal microtubules. In complex mammalian neurons, not only is the long distance a daunting task for transport, but the elaborate branches also pose a navigational challenge for targeted cargo delivery. Although recent studies have begun to elucidate the mechanisms regulating transport in different regions of a neuron (Britt et al., 2016; Guedes-Dias et al., 2019; Huang and Banker, 2012; Lipka et al., 2016; Nakata and Hirokawa, 2003; Nirschl et al., 2016; Zahavi and Hoogenraad, 2021), our understanding of how cargos navigate the branched architecture remains under-studied.

Most mammalian neurons develop multiple branches from their single axons to make synaptic connections at different destinations (Gibson and Ma, 2011; Kalil and Dent, 2014). The branched architecture is formed via multiple steps, including branch initiation, maturation, growth, guidance, and elimination, which are regulated by extracellular cues and neuronal activities (Gibson and Ma, 2011). Branches can remodel through competition (Kano and Hashimoto, 2009; Lichtman and Colman, 2000; Luo and O'Leary, 2005; Riccomagno and Kolodkin, 2015; Ruthazer et al., 2003; Schuldiner and Yaron, 2015) or in response to chemical or physical insults (Kerschensteiner et al., 2004; Tuszynski and Steward, 2012). Since each branch has unique structural and functional needs, the branch junctions pose potential "decision points" for cargos. Although transport inside branches has been investigated (Brill et al., 2016; Goldberg and Schacher, 1987; Ruthel and Hollenbeck, 2003), little is known about how transport is regulated through branch junctions. Are cargos transported randomly into each branch or is such transport regulated? If it is regulated, what controls which branch cargos move to? Can it be controlled by structural differences or functional changes farther away, such as in the growth cone (GC)? Moreover, is such regulation mediated by specific motors, as shown in the axon initial segment (AIS) (Gumy et al., 2017)?

To address these questions, we performed systematic transport analysis of three membrane cargos, LAMP1, synaptic, and BDNF vesicles, in cultured embryonic neurons from the dorsal root ganglion (DRG). We found that anterograde (Ant.) transport of LAMP1 and synaptic vesicles through branch junctions is not random; rather, it is selective and correlated with branch length and GC motility. Using local optogenetic manipulation, we demonstrated that GC signaling can rapidly alter the Ant. transport preference through branch junctions. Finally, we identified a role of KIF1/kinesin-3 in mediating this transport regulation. Our study thus provides strong evidence for selective transport at branch junctions that could have a wide influence on axonal branch development and function in the nervous system.

A

B   Branch junction

Branch

Common

Axon

C   Length

Transport Probability (%)

Axon   Branch

D

Transport into axon (%)

L_B/L_A

E   Caliber

W_B

W_A

Transport into axon (%)

W_B/W_A

F   Angle

θ_B

θ_A

Transport into axon (%)

θ_B/θ_A

G   GC motility

D

S

Transport into axon (%)

D/D   S/D   D/S
Branch/Axon

H   D/D   S/D   D/S

Transport into axon (%)

L_B/L_A (log10)

(legend on next page)

RESULTS

Anterograde transport of LAMP1 vesicles through branch junctions is selectively controlled by branch length and GC motility

We designed a live cell imaging assay to analyze vesicle transport when vesicles encounter axonal branch junctions in dissociated rat embryonic DRG neurons. We expressed fluorescently tagged LAMP1 to analyze late endosomes and lysosomes (Figure 1A), which are highly motile along axons (Cheng et al., 2018). Using iRFP670 (iRFP), a far-red marker (Shcherbakova and Verkhusha, 2013) to visualize axon morphology, we imaged LAMP1 in regions around the branch junctions (Figure 1A, magenta box): the common axon region before the branch junction (Figure 1A; blue line) and the two branches (Figure 1A, green and red lines). To simplify the discussion in the subsequent studies, we designated the longer branch as the axon and the shorter one as the branch (Figures 1A and 1B). From time-lapse movies (acquired every 0.5 s for 2 min), we generated kymographs (Figure 1B) to analyze LAMP1 movement through the branch junction (Figure 1A, magenta box). Using the LAMP1 trajectories on kymographs, we counted the Ant. transport events (aT_A or aT_B) through the branch junction (Figure 1B, right boxes, yellow dashed line) from the common axon region into either the axon (red) or the branch (green). For comparison, we counted the retrograde (Ret.) events (rT_A or rT_B) from either the axon or the branch.

From this analysis, we found that Ant. LAMP1 transport at branch junctions is not random but rather biased toward the axon. Out of an averaged total of 7.9 Ant. events ($aT_{Total} = aT_A + aT_B$) during the 2-min imaging window, 4.6 LAMP1 vesicles entered the axon and 3.3 entered the branch. The transport probability (expressed in percentage) into the axon ($aT_A\% = aT_A/aT_{Total}$) was 61% (Figure 1C), significantly different from 39% going into the branch (Figure 1C). Since the axon (20–300 μm, average of 92 μm) was 64% longer than the branch (11–200 μm, average of 52 μm), this result suggests that transport through branch junctions is biased or selective based on branch length. Ret. LAMP1 transport also showed a significant but smaller difference (Figure S1A) between the probabilities from the axon ($rT_A\% = 54\%$) and from the branch ($rT_B\% = 46\%$). These results show that the length difference between two branches at a branch junction can impact Ant. and Ret. LAMP1 transport.

To better understand the length effect, we plotted the Ant. transport probability into the axon ($aT_A\%$) against the length ratio of branch over axon (L_B/L_A) for each junction (Figure 1D). Using logistic regression, which models the odds or the ratio of transport into axon over branch ($aO_A = aT_A/aT_B$) as a function of the length ratio, we found a strong correlation. When L_B/L_A is 1 (branch and axon have equal length), the Ant. transport probability into axon is 51%, indicating that transport into the axon and the branch is nearly identical (Figure 1D). In contrast, at a branch junction where an axon is 10× or 2× longer than the branch ($L_B/L_A = 0.1$ or 0.5), the transport probability into axon is increased to 85% or 63% respectively. For comparison, the probability of Ret. transport from the axon ($rT_A\%$) is 52%, 55%, or 61% when L_B/L_A is 1, 0.5, or 0.1 (Figure S1B). These results reveal a clear influence of branch length on the Ant. LAMP1 transport selectivity.

We next analyzed the effect of two additional structural features, branch caliber and branch angle, which may determine the number and the curvature of microtubule tracks. To compare branch calibers, we measured the width (W_A and W_B) of the axon and branch segment 5–10 μm adjacent to the junction. When plotting against the caliber ratio of branch/axon (W_B/W_A), we found no correlation with Ant. LAMP1 transport into axons (Figure 1E). Similarly, Ant. transport showed no correlation with the ratio of the angle between the branch and the axon (Θ_B/Θ_A) (Figure 1F). Thus, neither branch caliber nor branch angle influences which branch LAMP1 vesicles enter.

In addition to the structural factors, we considered the role of dynamic factors, such as branch growth, which may have high demands for material synthesized in the cell body to be transported distally through branch junctions (Guedes-Dias and Holzbaur, 2019; Guillaud et al., 2020). We focused on GC motility, which is associated with branch growth (Dent and Gertler, 2003) and can be divided based on morphology into two groups: dynamic (D) versus static (S). Dynamic GCs have a spread lamellipodia with multiple filopodia, and static ones are either collapsed or stalled (Figure S1C). Using this characterization, we found an average of 5.0 Ant. transport events into axons with dynamic GCs and only 3.0 events with static GCs, equivalent to a probability of 64% versus 48% (Figures S1D and S1F). This significant difference was also seen for LAMP1 transport into branches, which have a higher number of transport events or probability when the branch GC was dynamic than static (Figures S1E and S1G). In contrast, the Ret. transport

---

Figure 1. Anterograde LAMP1 transport through branch junctions is influenced by branch length and GC motility

(A) Inverted fluorescence image of LAMP1-Emerald at a branch junction (magenta box) of a DRG neuron. Three regions surrounding the junction are marked by colored lines: common pre-junction axon (blue), branch (green), and axon (red).

(B) Kymograph (left panels) of LAMP1 movement between the common axon region and either the branch (top) or the axon (bottom) at the branch junction (magenta box) over a 2-min period. Transport trajectories (blue, green, and red lines) moving through the branch junction (yellow dashed line) are shown by schematic drawing (right panels).

(C–D) Impact of branch length on Ant. transport at branch junctions (n = 136). Quantification of the transport probability ($aT_A\%$, $aT_B\%$) into axon or branch (C) and plot of the probability into axon ($aT_A\%$) against the length ratio (L_B/L_A) (D). Logistic regression is shown by the dashed line.

(E–F) Plot of the Ant. transport probability into axon ($aT_A\%$) against the ratio of branch caliber (W_B/W_A) (E, n = 81) or angle (Θ_B/Θ_A) (F, n = 136). Logistic regression is shown by the dashed lines.

(G) Impact of GC motility on Ant. transport. Comparison of the transport probability into axon ($aT_A\%$) between three motility groups for branch and axon GCs: both dynamic (D/D, n = 62), static branch and dynamic axon (S/D, n = 48), and dynamic branch and static axon (D/S, n = 19).

(H) Logistic regression analysis of the Ant. transport probability ($aT_A\%$, n = 129) against both GC motility and the length ratio (L_B/L_A, in log10 scale). Logistic regression is shown by dashed lines for each GC motility group.

Scale bars: 10 μm. (C) Mann-Whitney test; (G) Kruskal-Wallis test. *p < 0.05; **p < 0.01; ***p < 0.005 ****p < 0.001. Error bars: SEM.

probability (rT$_A$% or rT$_B$%) from either axons or branches showed no difference between GCs with opposing motilities (Figures S1H and S1I). As a result, the Ant.:Ret. transport ratio (aT$_A$/rT$_A$ or aT$_B$/rT$_B$) exhibited a 2-fold increase between dynamic and static GCs from either axons or branches (Figures S1J and S1K). These results suggest that GC motility has a strong influence on Ant. transport regardless of whether it is associated with axon or branch.

We further compared the effect when GC motility of both the axon and the branch was analyzed. First, when GCs of the branch and the axon were both dynamic (designated as D/D), the probability of Ant. LAMP1 transported into the axon (aT$_A$%) was 58% (Figure 1G). The preference for the axon is consistent with the length influence observed earlier. However, when the branch GC was static but the axon GC was dynamic (designated as S/D), there was a large increase in the probability entering the axon (aT$_A$% = 72%; Figure 1G). In contrast, at the D/S junction where the branch GC was dynamic but the axon GC was static, there was a decrease of LAMP1 moving into the axon (aT$_A$% = 40%; Figure 1G). As before, Ret. transport showed no difference between any of these conditions (Figure S1L). Thus, Ant. LAMP1 transport is influenced by the GC motility of associated branches.

To understand the relative impact by GC motility versus branch length, we used logistical regression described earlier to model the Ant. transport odds (aO$_A$ = aT$_A$/aT$_B$) as a function of both GC motility (D or S) and branch length ratio (L$_B$/L$_A$). From the regression, we estimated the odds ratio (OR), i.e., how the transport odds change between different conditions, and used it to compare the impact (Figure 1H). After simultaneously controlling for GC motility and length ratio, the odds ratio (OR$_{D/S}$) between axons with dynamic and static GCs is 1.71 (Table S1; p = 0.022), indicating 71% higher transport odds (aO$_A$) into axons with dynamic GCs than those with static GCs. In contrast, the transport odds dropped by 32% when branch GCs changed from dynamic to static (Table S1; p = 0.014). For comparison, a 10% length difference has an odds ratio (OR$_{Length-A/B}$) of 1.06 (Table S1; p = 0.0001), equivalent to a 6% change in transport odds (aO$_A$). Based on the changes in aO$_A$, the impact by axon GC motility (D versus S) is similar to that of a 1.2-fold change of the length; and the impact of branch GC motility is similar to a 56% change of the length.
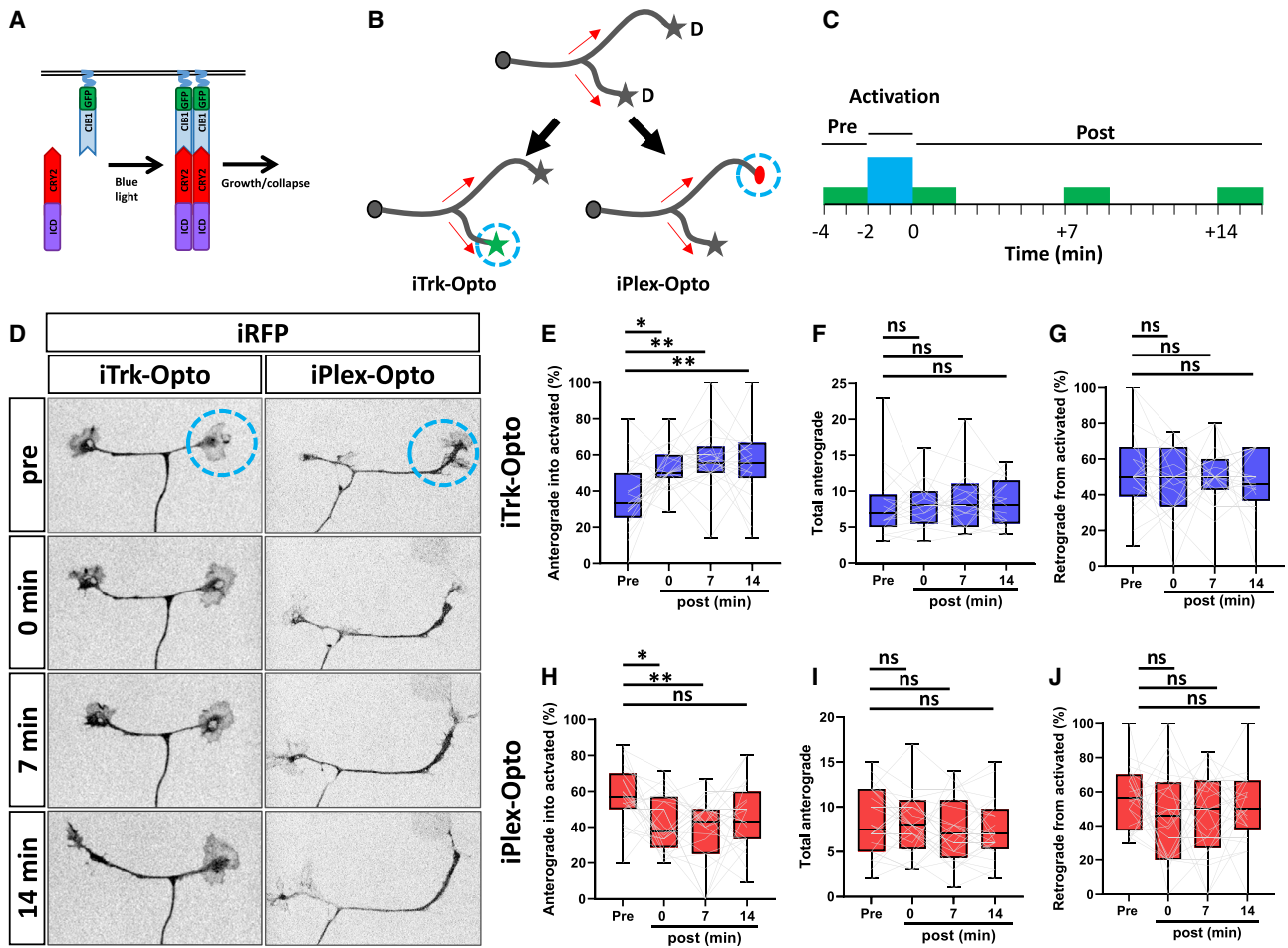
Moreover, the impact by branch length on Ant. transport into the axon (aO$_A$) appears remarkably similar for three GC motility groups (SD, DS, and DD): OR$_{Length-A/B}$ = 1.06, 1.02, and 1.06 (Table S1; also see parallel regression lines in Figure 1H). The similar effects of length ratio on all three conditions (Table S1; p = 0.848) suggest that the length impact does not interact with the impact by GC motility and hence little interaction between the structural and dynamic factors. Additionally, the effect on transport from axon GCs is statistically similar (Table S1; p = 0.546) to the effect from branch GCs, regardless of the GC motility of the branch, suggesting little interaction between the two GCs when influencing Ant. transport.

Taken together, our analysis of LAMP1 vesicles has revealed that Ant. transport through branch junctions is not random but instead influenced by branch length and more strongly by GC motility.

GC signaling rapidly alters anterograde transport selectivity through branch junctions

To understand how GCs control transport regulation through branch junctions, we employed a recently developed optogenetic system (Duan et al., 2018) to locally activate nerve growth factor (NGF)-dependent growth signaling. Here, a fusion protein (CRY2-iTrk) containing the intracellular domain (ICD) of the NGF receptor TrkA (iTrk) and the light-sensitive protein cryptochrome 2 (CRY2) were co-expressed with membrane-associated CIB1-GFP-CAAX. Blue light stimulation (480 nm) induced conformational change of CRY2 and heterodimerization of CRY2-iTrk with CIB1-GFP-CAAX (Figure 2A), leading to the activation of TrkA signaling and the subsequent promotion of neurite outgrowth (Duan et al., 2018). We generated an IRES2-based bicistronic construct (iTrk-Opto) for CRY2-iTrkA and CIB1-GFP-CAAX and expressed them in DRG neurons along with LAMP1-mCherry and iRFP. To maximize the effect of TrkA signaling, we cultured DRG neurons with reduced NGF (2 ng/mL) for 2 h prior to activation and analyzed branch junctions that have similar GC motility for both axons and branches (Figure 2B). We imaged LAMP1 movement for 2 min at 0.5-s intervals (Pre) and then locally exposed the branch GC with blue light every 10 s for 2 min (blue circle; Figures 2B and 2D). This was followed by LAMP1 imaging (Post) at the branch junction immediately after activation at 0 min, and then at 7 and 14 min (Figures 2C and 2D). In kymographs (Figure S2A), 37% (aT$_{Pre}$%) of Ant. LAMP1 transport entered the branch prior to activation (Figure 2E), consistent with the length effect on the transport into branches (Figure 1C). After activation, the transport probability into the activated branch (aT$_{Post}$%) rapidly increased to 52% within the first 2 min, and this increase persisted at 7 and 14 min (56%, 54%). Importantly, light activation did not affect the overall transport (Figure 2F), suggesting that the response is a redirection of LAMP1 transport through the branch junction, favoring the activated branch. Also, Ret. transport was not significantly affected (Figure 2G). To show specificity, we performed the same analysis with two control constructs: (1) Ctrl-Opto that lacks any CRY2-ICD and (2) K547N-iTrk-Opto that contains a K547N mutation known to inhibit the TrkA kinase activity (Amodeo et al., 2020). In both cases, we found no significant changes in the transport probability into or out of the activated branch or the total Ant. events before and after activation (Figures S2B–S2G). These results reveal that activation of TrkA signaling in GCs can influence Ant. LAMP1 transport at branch junctions.

To understand whether such transport regulation can be controlled by other signaling mechanisms, we next examined the effect of PlexinA4, a receptor known to mediate Semaphorin 3A-induced GC collapse and axon growth inhibition (Tamagnone et al., 1999; Winberg et al., 1998). We generated iPlex-Opto to express CIB1-GFP-CAAX and a CRY2 fusion with the ICD domain of PlexinA4 (iPlex), which can induce GC collapse (Mlechkovich et al., 2014). After co-expressing them with iRFP and LAMP1-mCherry in DRG neurons, we analyzed transport at branch junctions with two motile GCs. We chose to activate the GC of the axon, which normally has higher probability of LAMP1 transport into them (Figure 1C). As expected, 57% of lysosomes traveled into the axon (aT$_{Pre}$%) prior to light exposure (Figure 2H). However, within 2 min after light exposure, transport

Figure 2. Optogenetic manipulation of GC signaling rapidly alters anterograde LAMP1 transport through branch junctions

(A) Schematic illustration of the optogenetic system via the interaction between CRY2-ICD and CIB1-GFP-CAAX. Upon blue light activation, cytosolic CRY2-ICD binds to CIB1 and clusters at the plasma membrane to elicit receptor signaling responsible for GC growth or collapse.

(B–C) Experimental design (B) to analyze transport at branch junctions where one of the branches expressing iTrk-Opto or iPlex-Opto is activated by blue light and the time course (C) of 2-min transport imaging of LAMP1-mCherry (green bars) before (Pre) light activation (blue bar) or after (Post) at 0, 7, and 14 min.

(D) Inverted fluorescence images of branch junctions expressing iRFP and iTrk-Opto or iPlex-Opto at different times before or after light activation of one GC (blue circle). Scale bar: 20 μm.

(E–H) Quantification of the Ant. transport probability into the activated branch (E, H), the total number of Ant. transport (F, I), and the Ret. probability (G, J) from the activated branch before and after light exposure in neurons expressing iTrk-Opto (E–G, n = 21) or iPlex-Opto (H–J, n = 23). (E, G, H) Kruskal-Wallis; (F, I, J) one-way ANOVA. *p < 0.05; **p < 0.01, n.s., not significant. Error bars: SEM.

into the axon (aT$_{Post}$%) decreased to 42% and remained lower at 7 and 14 min (38%, 45%), suggesting that increased iPlex-Opto signaling altered transport through the branch junction. Again, the overall Ant. events did not change upon activation, nor did the Ret. transport probability (Figures 2I and 2J). As a further control, we tested a modified version of iPlex-Opto that lacks the KRK motif that is required for its repulsive activity (Mlechkovich et al., 2014). Activation of this ΔKRK-iPlex-Opto construct was unable to alter the LAMP1 transport probability in both Ant. and Ret. directions (Figures S2H–S2J), suggesting the requirement of PlexinA4 signaling. Taken together, these results demonstrate that growth stimulatory or inhibitory signaling in GCs can rapidly change Ant. transport through branch junctions by redirecting transport into specific branches.

Differential regulation of transport selectivity by GCs for synaptic and BDNF vesicles

To determine if the transport selectivity seen with LAMP1 was applicable to other cargos, we next analyzed synaptic and BDNF vesicles, two vesicles known to be transported along axons (Colin et al., 2008; Okada et al., 1995). Using synaptophysin-EGFP (Syn-EGFP) (Hruska et al., 2018) to analyze the same parameters described earlier (yellow line; Figure 3A), we found that synaptic vesicles behaved in a similar way to LAMP1 vesicles, showing a strong response to GC motility (Figures 3A and 3B). When GCs were both dynamic (D/D), Syn-EGFP was evenly distributed between the axon and the branch (aT$_A$% = 51%); when the GC has opposite motility behaviors between the branch and the axon, there was a strong influence on selectivity: transport into the axon is 75%
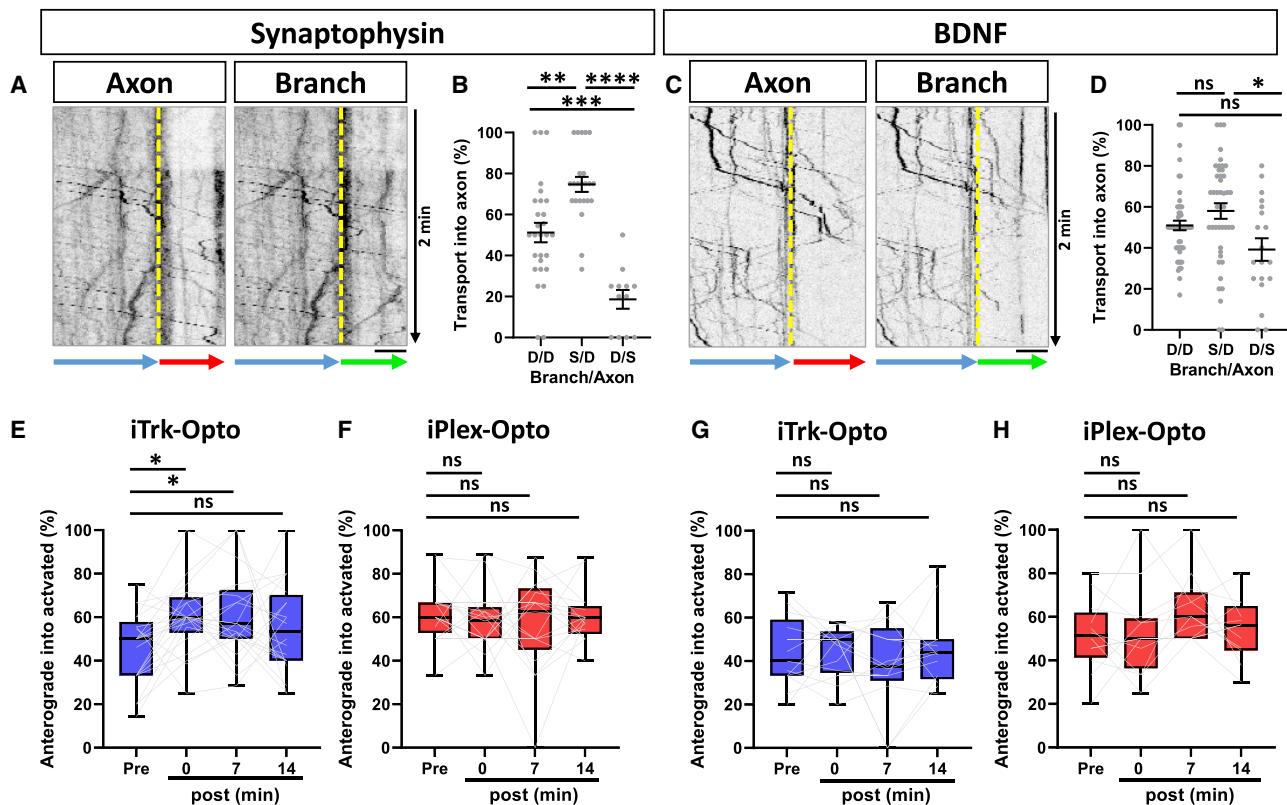
Figure 3. Selective anterograde transport of synaptic, but not BDNF, vesicles is influenced by GC motility

(A–D) Inverted kymograph of synaptophysin-GFP vesicles (A) or BDNF-mRFP vesicles (C) through the branch junction (yellow line) from the common axon (blue lines) into the axon (red lines) or the branch (green lines). Comparison of the Ant. transport probability of synaptic (B, n = 63) or BDNF (D, n = 116) vesicles into the axon based on the GC motility of branch versus axon. Scale bars: 20 μm.

(E–H) Quantification of the Ant. transport probability of synaptophysin (E, F, n = 21 or 17) or BDNF (G, H, n = 13 or 12) vesicles through the branch junction before and after optogenetic activation of one GC expressing iTrk-Opto (E, G) or iPlex-Opto (F, H).

(B, D, F, G) Kruskal-Wallis; (E, H) one-way ANOVA. *p < 0.05; **p < 0.01; ***p < 0.001; ****p < 0.0001, n.s., not significant. Error bars: SEM.

for the S/D junctions and 19% for the D/S junctions. Consistently, analysis by logistic regression (Figure S3A, Table S1) reveals that the length impact is minimal, with a 2% increase (p = 0.207) in O_A for 10% change in the length ratio. In contrast, the transport probability into axons with dynamic GCs is 3.37-fold (p = 0.001) higher than those with static GCs, and it drops by 60% (p = 0.001) when branch GCs are changed from static to dynamic (Table S1). Consequently, the impact by GC motility is equivalent to that of ~12-fold length difference between the axon and the branch (Table S1). In contrast, there was no effect of GC motility on the Ret. transport probability (Figure S3B). Thus, the Ant. transport selectivity of synaptic vesicles is strongly influenced by GC motility.

We next examined BDNF vesicles using BDNF-mRFP (Yang et al., 2019) (Figure 3C) and found that their Ant. transport showed little response to either branch length or GC motility (Figures 3D and S3C). The significant impact of GC motility seen in LAMP1 and synaptic vesicles was severely reduced (Figure 3D) (aT_A% = 58% for S/D; aT_A% = 39% for D/S) when compared to similar GCs (aT_A% = 51% for D/D). Analysis by logistic regression confirms a reduced impact by GC motility and an insignificant impact by branch length (Table S1). Similarly, their Ret. transport was not affected by GC motility (Figure S3D).

To examine the impact of GC signaling, we analyzed transport of these two vesicles in response to optogenetic manipulation of iTrk-Opto or iPlex-Opto. iTrk-Opto elicited a positive response of Syn-DsRed-labeled vesicles, increasing their transport into the activated branch (Figure 3E). Prior to activation, 45% (aT_{Pre}%) of Syn-DsRed moved into the branch. After activation, Syn-DsRed transport (aT_{Post}%) increased to 60% and remained at this level at 7 min before decreasing to 54% at 14 min (Figure 3E). Interestingly, iPlex-Opto had no effect on Syn-DsRed transport, eliciting insignificant changes between the pre-activation level (aT_{Pre}% = 62%) and the post-activation levels (aT_{Post}% = 56% or 60% at 7 or 14 min) (Figure 3F). Consistent with the limited effect of GC motility, BDNF showed no response to either iTrk-Opto or iPlex-Opto activation (Figures 3G and 3H). Under both conditions, BDNF transport into the activated branch did not significantly differ from the pre-activation levels. For both Syn and BDNF vesicles, there was no change in the total Ant. transport events (Figures S3E–S3H), again suggesting that optogenetic activation does not affect the overall transport. Also, there was no change in Ret. transport after activation (not shown). These results demonstrate that transport selectivity is dynamically regulated by GCs, but not all vesicles are regulated in the same way.

KIF1/kinesin-3, not KIF5/kinesin-1, mediates signaling-dependent transport selectivity at branch junctions

The difference of transport selectivity observed for different vesicles may reflect the motor proteins used for their transport. It has been suggested that synaptic vesicles are predominantly transported by the plus end directed motor KIF1/kinesin-3 (Hall and Hedgecock, 1991; Hummel and Hoogenraad, 2021; Okada et al., 1995; Pack-Chung et al., 2007), BDNF vesicles by KIF5/kinesin-1 (Butowt and von Bartheld, 2007; Colin et al., 2008), and LAMP1-labeled late endosomes and lysosomes by both KIF1 and KIF5 (Guardia et al., 2016; Mohan et al., 2019). Since Ant. transport of both synaptic and LAMP1 vesicles is influenced by GC motility and signaling, we hypothesized that KIF1 was the main motor mediating transport selectivity.

To test this hypothesis, we first examined the behavior of truncated motors, KIF1(1–393) and KIF5(1–560), which are constitutively active (CA) and lack the ability to interact with vesicles (Friedman and Vale, 1999; Jacobson et al., 2006). We used fluorescence recovery after photo bleaching (FRAP) to estimate the transport kinetics of these motors to the GC with different motility behaviors (Figures S4A–S4C). Analysis of the amplitude of KIF1-CA FRAP revealed a greater level of recovery in dynamic GCs compared with static GCs (79% versus 38%; Figure S4B). This was also seen for KIF5-CA, recovering more in dynamic than static GCs (46% versus 16%, Figure S4C). Assuming negligible changes in diffusion, this result suggests that branch GC motility affects kinesin motors traveling along the axon independent of the vesicles they bind.

Since KIF1 and KIF5 move on microtubules at different velocities (1.5 μm/s versus 1 μm/s), and both bind LAMP1 vesicles (Figure 4A), we asked if we could use velocities to determine which kinesins were actively transporting LAMP1 in response to GC signaling in the aforementioned optogenetic experiments. Prior to activation, the average LAMP1 velocity in iTrk-Opto neurons was 1.1 μm/s for both activated and control branches (Figure 4B), suggesting that both kinesins are active. Interestingly, immediately after activation, the average velocities increased in the activated branch but decreased in the control branch, suggesting a potential change in KIF1 or KIF5 engaged LAMP1 movement. Conversely, in the iPlex-Opto activation experiment (Figure 4C), both activated and control branches showed a decrease in velocities that gradually recovered overtime. These results hint that GC signaling may shift motor usage, altering between KIF1 and KIF5 in transporting LAMP1 vesicles.

To determine whether KIF1 is indeed responsible, we asked if knocking down KIF1 could affect vesicle transport induced by GC signaling. To achieve this, we generated shRNA constructs targeting two KIF1 isoforms (1A and 1B) based on the previously verified targeting sequences (Lipka et al., 2016; Pan et al., 2019). For comparison, we generated shRNA constructs for three KIF5 isoforms (5A, 5B, 5C). We chose to analyze LAMP1 vesicles because they are bound by both kinesins (Guardia et al., 2016; Mohan et al., 2019). Moreover, knockdown of either family of motors did not abolish their overall transport at branch junctions (Figures 4E, 4G, 4I, and 4K), thus allowing the shift of the balance of the two families of kinesins available on LAMP1 vesicles. Using this strategy, we first tested the effect of KIF1 or KIF5 knockdown on the LAMP1 transport in the iTrk-Opto system

(Figures 4D, 4H, and S4D). With KIF1 knockdown, the total Ant. LAMP1 transport was not affected (Figure 4E), and transport into branches (aT$_{Pre}$%) was 47% prior to activation (Figure 4D). However, iTrk-Opto activation in the branch GC did not significantly alter the transport into the activated branches (aT$_{Post}$%), which remained at 43% at 0 and 7 min or 48% at 14 min (Figure 4D), suggesting that KIF1 knockdown abolished signal-induced transport selectivity seen earlier (Figure 2E). In contrast, after KIF5 knockdown, LAMP1 transport into branches still increased after iTrkA activation, from 34% pre-activation to 50%–55% post-activation (Figure 4H) without affecting the total transport (Figure 4I), indicating that KIF5 knockdown had little impact on transport selectivity. Similarly, knockdown of KIF1 but not KIF5 affects iPlex-Opto stimulated transport changes without affecting the total events (Figures 4F–4G, 4J–4K, and S4D). Taken together, these data support the role of KIF1 but not KIF5 in regulating Ant. transport through branch junctions in response to GC signaling.

DISCUSSION

Neurons often have highly branched morphologies that are essential for neuronal functions (Gibson and Ma, 2011; Kalil and Dent, 2014), but little is known about how cargos navigate the branched architecture to reach their destination. By studying three membrane vesicles in DRG axons, we demonstrate that Ant. transport at branch junctions is not random but rather selective. Importantly, we have identified both structural (branch length) and dynamic (GC motility) factors that regulate transport selectivity (Figures 1 and 3). Analysis by logistic regression reveals that dynamic factors have a stronger influence on transport selectivity, as the impact of GC motility is equivalent to that of a 1.2-fold length difference for LAMP1 vesicles or 12-fold length difference for synaptic vesicles. Such dynamic regulation of transport selectivity is further supported by the manipulation of GC signaling using optogenetic tools (Figure 2).

Since GCs are responsible for receiving and integrating extracellular signals to guide axon growth, the ability to regulate selective transport at branch junctions in response to GC signaling is paramount to the development of branched neural networks. It enables neurons to deliver different proteins and membrane cargos to growing branches during early development (Kalil and Dent, 2014) or to competing branches undergoing remodeling (Brill et al., 2016). This mechanism of selective transport thus adds another layer of cellular regulation for axonal development. Moreover, such transport regulation could impact the sprouting responses after nerve injury (Curcio and Bradke, 2018; Tuszynski and Steward, 2012).

Our study also identified a potential motor mechanism mediating transport selectivity. Analysis of transport speed suggests that KIF1 but not KIF5 mediates selective transport. Moreover, shRNA knockdown demonstrates the requirement of KIF1 but not KIF5 for signal-dependent transport selectivity of LAMP1 vesicles (Figure 4). In line with the role of KIF1 in sorting transport at the AIS (Gumy et al., 2017; Leterrier and Dargent, 2014; Zahavi and Hoogenraad, 2021), our results further suggest that some motors (e.g., KIF5) drive forward movement, while other motors (e.g., KIF1) steer transport along microtubule tracks. Such regulation
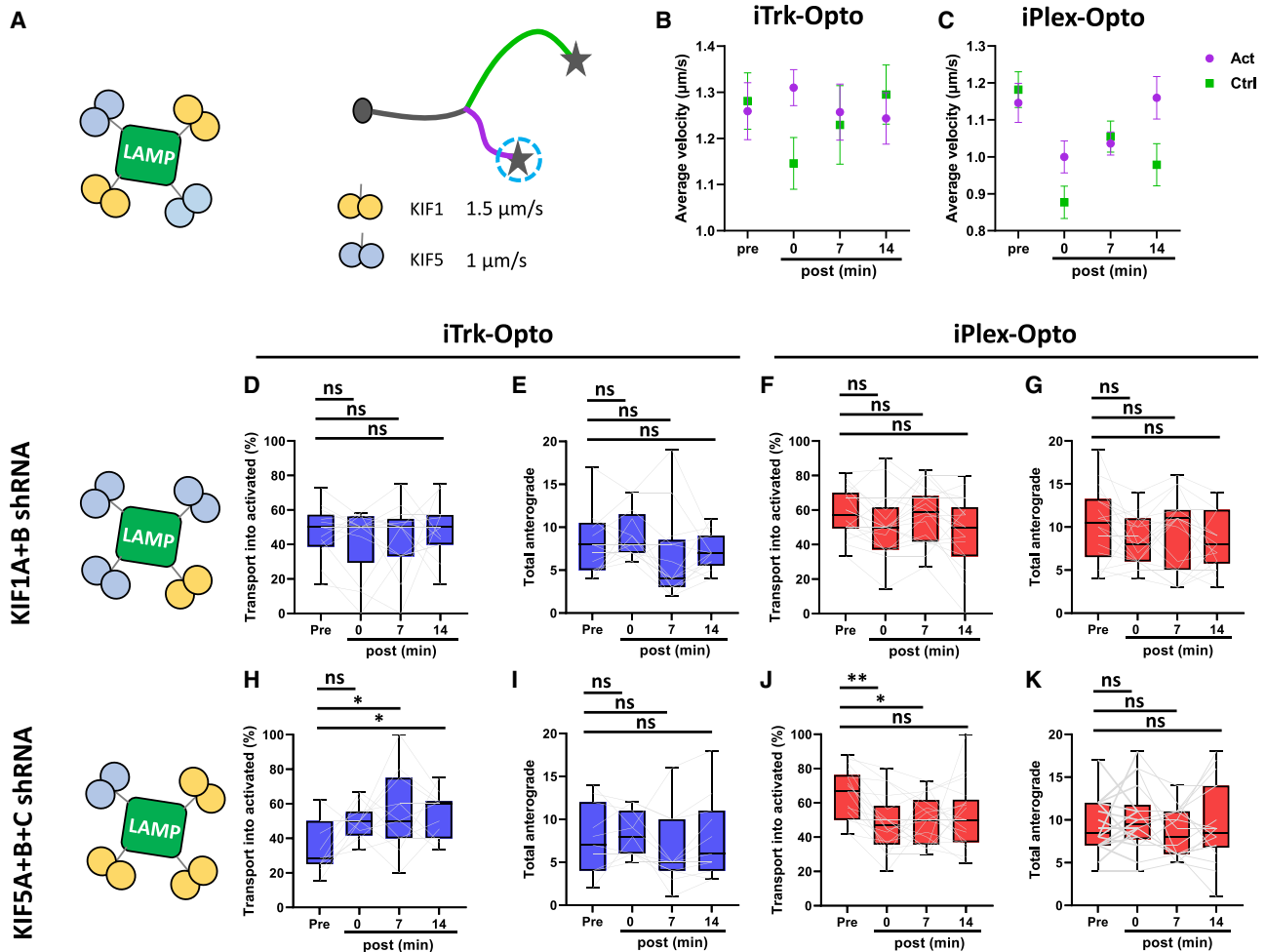
Figure 4. KIF1/Kinesin-3 motors mediate anterograde LAMP1 transport selectivity through branch junctions in response to activation of GC signaling

(A) Schematic of the motors associated with LAMP1 vesicles and the regions of the neurons where the transport velocities were recorded. Reported average speeds of KIF1 and KIF5 are shown.

(B–C) Quantification of average Ant. LAMP1 velocities in activated (Act, magenta circles) or control (Ctrl, green squares) branches expressing iTrk-Opto (B) or iPlex-Opto (C). n = 36–75.

(D–K) Quantification of the Ant. LAMP1 transport probability into activated branches (D, F, H, J) and the total number of Ant. transport- (E, G, I, K) at the branch junction of neurons expressing iTrk-Opto (D–E, n = 11, H–I, n = 13) or iPlex-Opto (F–G, J–K, n = 18) along with shRNAs to knock down KIF1A/B (D–G) or KIF5A/B/C (H–K). (D, E, G, I) Kruskal-Wallis; (F, H, J) one-way ANOVA. *p < 0.05; **p < 0.01, n.s., not significant. Error bars: SEM.

could be achieved at several possible sites, including motor-vesicle coupling (Hummel and Hoogenraad, 2021), motor activity (Atherton et al., 2020), post-translational modifications of microtubules (Guedes-Dias et al., 2019), and various microtubule-associated proteins (Monroy et al., 2018; Tymanskyj et al., 2018). Identifying the sites of regulation in the future would help understand how transport selectivity is controlled by GC signaling.

Our study is based on the analysis of three vesicles, but the selective transport regulation may represent a common feature at branch junctions. In fact, we have noticed that Ret. LAMP1 transport is also sensitive to branch length (Figure S1B), and not all vesicles are influenced by GC motility and signaling in the same way (Figures 1, 2, and 3). These differences suggest that transport selectivity is applicable to other protein or membrane

cargos, but the regulation may depend on the functional needs at branch terminals. For example, mature neurons containing shorter localized arbors and long projecting axons could use a selective transport mechanism to ensure efficient delivery of mitochondria and other cargos for synaptic function and maintenance (Smith and Gallo, 2018; Winkle et al., 2016). More importantly, such transport regulation might be influenced by other factors, such as synaptic activity and nerve injury (Hausott and Klimaschewski, 2016; Rizalar et al., 2021). For example, synaptic activities could use a similar mechanism to influence transport of synaptic function-related cargos through branch junctions (Alpizar et al., 2019; Guedes-Dias and Holzbaur, 2019), or nerve injury might alter the transport of autophagosomes through branch junctions (Crawley and Grill, 2021; Murillo and Mendes Sousa,

2018). Selective transport could thus provide a mechanism to support neuronal plasticity and respond to nerve injury. Thus, we believe that this transport regulation has a broad influence of axonal development, plasticity, and regeneration.

Limitations of the study

Our study is limited to the analysis of three membrane cargos in rat embryonic DRG neurons. Based on several defined parameters, such as branch length and GC motility, our unbiased analyses have uncovered a regulatory feature for Ant. transport at branch junctions. We anticipate that similar regulation is likely common to other cargos in other neuronal cells, but further studies are needed. Moreover, our observation is based on the study of transport in axons, and it would be interesting to see whether similar regulation happens in dendrites. Finally, our conclusion is derived from the study of neurons in culture, and we postulate that similar transport regulation operates *in vivo* to support neuronal development and function.

STAR★METHODS

Detailed methods are provided in the online version of this paper and include the following:

- KEY RESOURCES TABLE
- RESOURCE AVAILABILITY
  - Lead contact
  - Materials availability
  - Data and code availability
- EXPERIMENTAL MODEL AND SUBJECT DETAILS
- METHOD DETAILS
  - DNA construct generation
  - DRG neuron culture
  - Live cell imaging
  - Image analysis and quantification
- QUANTIFICATION AND STATISTICAL ANALYSIS

REFERENCES

Alpizar, S.A., Cho, I.H., and Hoppa, M.B. (2019). Subcellular control of membrane excitability in the axon. Curr. Opin. Neurobiol. *57*, 117–125.

Amodeo, R., Nifosi, R., Giacomelli, C., Ravelli, C., La Rosa, L., Callegari, A., Trincavelli, M.L., Mitola, S., Luin, S., and Marchetti, L. (2020). Molecular insight on the altered membrane trafficking of TrkA kinase dead mutants. Biochim. Biophys. Acta Mol. Cell Res. *1867*, 118614.

Atherton, J., Hummel, J.J., Olieric, N., Locke, J., Pena, A., Rosenfeld, S.S., Steinmetz, M.O., Hoogenraad, C.C., and Moores, C.A. (2020). The mechanism of kinesin inhibition by kinesin-binding protein. Elife *9*, e61481.

Bindels, D.S., Haarbosch, L., van Weeren, L., Postma, M., Wiese, K.E., Mastop, M., Aumonier, S., Gotthard, G., Royant, A., Hink, M.A., et al. (2017). mScarlet: a bright monomeric red fluorescent protein for cellular imaging. Nat. Methods *14*, 53–56.

Brill, M.S., Kleele, T., Ruschkies, L., Wang, M., Marahori, N.A., Reuter, M.S., Hausrat, T.J., Weigand, E., Fisher, M., Ahles, A., et al. (2016). Branch-specific microtubule destabilization mediates axon branch loss during neuromuscular synapse elimination. Neuron *92*, 845–856.

Britt, D.J., Farias, G.G., Guardia, C.M., and Bonifacino, J.S. (2016). Mechanisms of polarized organelle distribution in neurons. Front. Cell Neurosci. *10*, 88.

Butowt, R., and von Bartheld, C.S. (2007). Conventional kinesin-I motors participate in the anterograde axonal transport of neurotrophins in the visual system. J. Neurosci. Res. *85*, 2546–2556.

Cheng, X.T., Xie, Y.X., Zhou, B., Huang, N., Farfel-Becker, T., and Sheng, Z.H. (2018). Characterization of LAMP1-labeled nondegradative lysosomal and endocytic compartments in neurons. J. Cell Biol. *217*, 3127–3139.

Colin, E., Zala, D., Liot, G., Rangone, H., Borrell-Pages, M., Li, X.J., Saudou, F., and Humbert, S. (2008). Huntingtin phosphorylation acts as a molecular switch for anterograde/retrograde transport in neurons. EMBO J. *27*, 2124–2134.

Courchet, J., Lewis, T.L., Jr., Lee, S., Courchet, V., Liou, D.Y., Aizawa, S., and Polleux, F. (2013). Terminal axon branching is regulated by the LKB1-NUAK1 kinase pathway via presynaptic mitochondrial capture. Cell *153*, 1510–1525.

Crawley, O., and Grill, B. (2021). Autophagy in axonal and presynaptic development. Curr. Opin. Neurobiol. *69*, 139–148.

Curcio, M., and Bradke, F. (2018). Axon regeneration in the central nervous system: facing the challenges from the inside. Annu. Rev. Cell Dev. Biol. *34*, 495–521.

Dent, E.W., and Gertler, F.B. (2003). Cytoskeletal dynamics and transport in growth cone motility and axon guidance. Neuron *40*, 209–227.

Duan, L., Hope, J.M., Guo, S., Ong, Q., Francois, A., Kaplan, L., Scherrer, G., and Cui, B. (2018). Optical activation of TrkA signaling. ACS Synth. Biol. *7*, 1685–1693.

Friedman, D.S., and Vale, R.D. (1999). Single-molecule analysis of kinesin motility reveals regulation by the cargo-binding tail domain. Nat. Cell Biol. *1*, 293–297.

Gibson, D.A., and Ma, L. (2011). Developmental regulation of axon branching in the vertebrate nervous system. Development *138*, 183–195.

Goldberg, D.J., and Schacher, S. (1987). Differential growth of the branches of a regenerating bifurcate axon is associated with differential axonal transport of organelles. Dev. Biol. *124*, 35–40.

Guardia, C.M., Farias, G.G., Jia, R., Pu, J., and Bonifacino, J.S. (2016). BORC functions upstream of kinesins 1 and 3 to coordinate regional movement of lysosomes along different microtubule tracks. Cell Rep. *17*, 1950–1961.

Guedes-Dias, P., and Holzbaur, E.L.F. (2019). Axonal transport: driving synaptic function. Science *366*, eaaw9997.

Guedes-Dias, P., Nirschl, J.J., Abreu, N., Tokito, M.K., Janke, C., Magiera, M.M., and Holzbaur, E.L.F. (2019). Kinesin-3 responds to local microtubule dynamics to target synaptic cargo delivery to the presynapse. Curr. Biol. *29*, 268–282.e8.

Guillaud, L., El-Agamy, S.E., Otsuki, M., and Terenzio, M. (2020). Anterograde Axonal transport in neuronal homeostasis and disease. Front. Mol. Neurosci. *13*, 556175.

Gumy, L.F., Katrukha, E.A., Grigoriev, I., Jaarsma, D., Kapitein, L.C., Akhmanova, A., and Hoogenraad, C.C. (2017). MAP2 defines a pre-axonal filtering zone to regulate KIF1- versus KIF5-dependent cargo transport in sensory neurons. Neuron *94*, 347–362.e7.

Hall, D.H., and Hedgecock, E.M. (1991). Kinesin-related gene unc-104 is required for axonal transport of synaptic vesicles in C. elegans. Cell *65*, 837–847.

Hausott, B., and Klimaschewski, L. (2016). Membrane turnover and receptor trafficking in regenerating axons. Eur. J. Neurosci. *43*, 309–317.

Hruska, M., Henderson, N., Le Marchand, S.J., Jafri, H., and Dalva, M.B. (2018). Synaptic nanomodules underlie the organization and plasticity of spine synapses. Nat. Neurosci. *21*, 671–682.

Huang, C.F., and Banker, G. (2012). The translocation selectivity of the kinesins that mediate neuronal organelle transport. Traffic *13*, 549–564.

Hummel, J.J.A., and Hoogenraad, C.C. (2021). Specific KIF1A-adaptor interactions control selective cargo recognition. J. Cell Biol. *220*, e202105011.

Jacobson, C., Schnapp, B., and Banker, G.A. (2006). A change in the selective translocation of the Kinesin-1 motor domain marks the initial specification of the axon. Neuron *49*, 797–804.

Kalil, K., and Dent, E.W. (2014). Branch management: mechanisms of axon branching in the developing vertebrate CNS. Nat. Rev. Neurosci. *15*, 7–18.

Kano, M., and Hashimoto, K. (2009). Synapse elimination in the central nervous system. Curr. Opin. Neurobiol. *19*, 154–161.

Kerschensteiner, M., Bareyre, F.M., Buddeberg, B.S., Merkler, D., Stadelmann, C., Bruck, W., Misgeld, T., and Schwab, M.E. (2004). Remodeling of axonal connections contributes to recovery in an animal model of multiple sclerosis. J. Exp. Med. *200*, 1027–1038.

Leterrier, C., and Dargent, B. (2014). No Pasaran! Role of the axon initial segment in the regulation of protein transport and the maintenance of axonal identity. Semin. Cell Dev. Biol. *27*, 44–51.

Lichtman, J.W., and Colman, H. (2000). Synapse elimination and indelible memory. Neuron *25*, 269–278.

Lipka, J., Kapitein, L.C., Jaworski, J., and Hoogenraad, C.C. (2016). Microtubule-binding protein doublecortin-like kinase 1 (DCLK1) guides kinesin-3-mediated cargo transport to dendrites. EMBO J. *35*, 302–318.

Luo, L., and O'Leary, D.D. (2005). Axon retraction and degeneration in development and disease. Annu. Rev. Neurosci. *28*, 127–156.

Mlechkovich, G., Peng, S.S., Shacham, V., Martinez, E., Gokhman, I., Minis, A., Tran, T.S., and Yaron, A. (2014). Distinct cytoplasmic domains in Plexin-A4 mediate diverse responses to semaphorin 3A in developing mammalian neurons. Sci. Signal. *7*, ra24.

Mohan, N., Sorokina, E.M., Verdeny, I.V., Alvarez, A.S., and Lakadamyali, M. (2019). Detyrosinated microtubules spatially constrain lysosomes facilitating lysosome-autophagosome fusion. J. Cell Biol. *218*, 632–643.

Monroy, B.Y., Sawyer, D.L., Ackermann, B.E., Borden, M.M., Tan, T.C., and Ori-McKenney, K.M. (2018). Competition between microtubule-associated proteins directs motor transport. Nat. Commun. *9*, 1487.

Murillo, B., and Mendes Sousa, M. (2018). Neuronal intrinsic regenerative capacity: the impact of microtubule organization and axonal transport. Dev. Neurobiol. *78*, 952–959.

Nakata, T., and Hirokawa, N. (2003). Microtubules provide directional cues for polarized axonal transport through interaction with kinesin motor head. J. Cell Biol. *162*, 1045–1055.

Nirschl, J.J., Ghiretti, A.E., and Holzbaur, E.L.F. (2016). Lipid rafts assemble dynein ensembles. Trends Biochem. Sci. *41*, 393–394.

Okada, Y., Yamazaki, H., Sekine-Aizawa, Y., and Hirokawa, N. (1995). The neuron-specific kinesin superfamily protein KIF1A is a unique monomeric motor for anterograde axonal transport of synaptic vesicle precursors. Cell *81*, 769–780.

Pack-Chung, E., Kurshan, P.T., Dickman, D.K., and Schwarz, T.L. (2007). A Drosophila kinesin required for synaptic bouton formation and synaptic vesicle transport. Nat. Neurosci. *10*, 980–989.

Pan, X., Cao, Y., Stucchi, R., Hooikaas, P.J., Portegies, S., Will, L., Martin, M., Akhmanova, A., Harterink, M., and Hoogenraad, C.C. (2019). MAP7D2 localizes to the proximal axon and locally promotes kinesin-1-mediated cargo transport into the axon. Cell Rep. *26*, 1988–1999.e6.

Riccomagno, M.M., and Kolodkin, A.L. (2015). Sculpting neural circuits by axon and dendrite pruning. Annu. Rev. Cell Dev. Biol. *31*, 779–805.

Rizalar, F.S., Roosen, D.A., and Haucke, V. (2021). A presynaptic perspective on transport and assembly mechanisms for synapse formation. Neuron *109*, 27–41.

Ruthazer, E.S., Akerman, C.J., and Cline, H.T. (2003). Control of axon branch dynamics by correlated activity in vivo. Science *301*, 66–70.

Ruthel, G., and Hollenbeck, P.J. (2003). Response of mitochondrial traffic to axon determination and differential branch growth. J. Neurosci. *23*, 8618–8624.

Schuldiner, O., and Yaron, A. (2015). Mechanisms of developmental neurite pruning. Cell Mol. Life Sci. *72*, 101–119.

Shcherbakova, D.M., and Verkhusha, V.V. (2013). Near-infrared fluorescent proteins for multicolor in vivo imaging. Nat. Methods *10*, 751–754.

Smith, G.M., and Gallo, G. (2018). The role of mitochondria in axon development and regeneration. Dev. Neurobiol. *78*, 221–237.

Tamagnone, L., Artigiani, S., Chen, H., He, Z., Ming, G.I., Song, H., Chedotal, A., Winberg, M.L., Goodman, C.S., Poo, M., et al. (1999). Plexins are a large family of receptors for transmembrane, secreted, and GPI-anchored semaphorins in vertebrates. Cell *99*, 71–80.

Tuszynski, M.H., and Steward, O. (2012). Concepts and methods for the study of axonal regeneration in the CNS. Neuron *74*, 777–791.

Tymanskyj, S.R., Yang, B., Falnikar, A., Lepore, A.C., and Ma, L. (2017). MAP7 regulates axon collateral branch development in dorsal root ganglion neurons. J. Neurosci. *37*, 1648–1661.

Tymanskyj, S.R., Yang, B.H., Verhey, K.J., and Ma, L. (2018). MAP7 regulates axon morphogenesis by recruiting kinesin-1 to microtubules and modulating organelle transport. Elife *7*, e36374.

Winberg, M.L., Noordermeer, J.N., Tamagnone, L., Comoglio, P.M., Spriggs, M.K., Tessier-Lavigne, M., and Goodman, C.S. (1998). Plexin A is a neuronal semaphorin receptor that controls axon guidance. Cell *95*, 903–916.

Winkle, C.C., Taylor, K.L., Dent, E.W., Gallo, G., Greif, K.F., and Gupton, S.L. (2016). Beyond the cytoskeleton: the emerging role of organelles and membrane remodeling in the regulation of axon collateral branches. Dev. Neurobiol. *76*, 1293–1307.

Yang, R., Bostick, Z., Garbouchian, A., Luisi, J., Banker, G., and Bentley, M. (2019). A novel strategy to visualize vesicle-bound kinesins reveals the diversity of kinesin-mediated transport. Traffic *20*, 851–866.

Zahavi, E.E., and Hoogenraad, C.C. (2021). Multiple layers of spatial regulation coordinate axonal cargo transport. Curr. Opin. Neurobiol. *69*, 241–246.

Zhao, Z., Wang, Z., Gu, Y., Feil, R., Hofmann, F., and Ma, L. (2009). Regulate axon branching by the cyclic GMP pathway via inhibition of glycogen synthase kinase 3 in dorsal root ganglion sensory neurons. J. Neurosci. *29*, 1350–1360.

STAR★METHODS

KEY RESOURCES TABLE

REAGENT or RESOURCE	SOURCE	IDENTIFIER
Recombinant DNA		
LAMP1-mEmerald	(Courchet et al., 2013)	N/A
LAMP1-mCherry	This paper	N/A
iTrk-Opto	This paper	N/A
iPlex-Opto	This paper	N/A
Ctrl-Opto	This paper	N/A
K547N-iTRK-Opto	This paper	N/A
ΔKRK-iPlex-Opto	This paper	N/A
Synaptophysin (Syn)-EGFP	(Hruska et al., 2018)	N/A
Synaptohpysin (Syn)-DsRed	(Hruska et al., 2018)	N/A
BDNF-mRFP	(Yang et al., 2019)	N/A
KIF1-CA-mScarlet	This paper	N/A
KIF5-CA-mScarlet	This paper	N/A
iRFP	(Tymanskyj et al., 2018)	N/A
KIF1A shRNA-iRFP	This paper: GACCGGACCTTCTACCAGT Sequence from (Lipka et al., 2016)	N/A
KIF1B shRNA- iRFP	This paper: GCAACGCTGTTATCAATGA Sequence from (Lipka et al., 2016)	N/A
KIF5A shRNA- iRFP	This paper: GAGACATCTTCAACCACAT Sequence from (Pan et al., 2019)	N/A
KIF5B shRNA- iRFP	This paper: TGGAGGGTAAACTTCATGA Sequence from (Pan et al., 2019)	N/A
KIF5C shRNA- iRFP	This paper: TGAGATCTACTTGGACAAA Sequence from (Pan et al., 2019)	N/A
CRY2-mCherry-iTrkA	Addgene	#106168
pmScarlet-i_C1	Addgene	#85044
pIRES2-EGFP	Clontech (Takara)	N/A
Software and algorithms		
Prism 9	GraphPad Software	https://www.graphpad.com/scientific-software/prism/
ImageJ	NIH	https://ImageJ.nih.gov/ij/

RESOURCE AVAILABILITY

Lead contact
Further information and requests for resources should be directed to and will be fulfilled by the lead contact, Le Ma (le.ma@jefferson.edu).

Materials availability
All unique reagents generated in this study are available from the lead contact with a completed materials transfer agreement.

Data and code availability
- All data reported in this paper will be shared by the lead contact upon request.
- This paper does not report the original code.
- Any additional information required to reanalyze the data reported in this paper is available from the lead contact upon request.

EXPERIMENTAL MODEL AND SUBJECT DETAILS

Timed pregnant Sprague Dawley rats were obtained from Charles River and used in accordance with the Guidelines for the Care and Use of Laboratory Animals of the National Institutes of Health and the approved IACUC protocol (#01560) of the Thomas Jefferson University. Vaginal plug dates were designated as E0. Embryos of both sexes were combined for each experiment.

METHOD DETAILS

DNA construct generation

LAMP1-mCherry was generated by subcloning LAMP1 from the LAMP1-mEmerald vector (gift from Dr. Franck Polleux (Courchet et al., 2013)) to a pCAGGS-mCherry vector using the XbaI and EcoRI sites. Syn-EGFP and -DsRed were gifts from Dr. Martin Hruska. BDNF-mRFP was a gift from Dr. Gary Banker.

The optogenetic vectors were generated as the following. The Ctrl-Opto construct was created by subcloning CIB1-GFP-CAAX (gift from Dr. Bianxiao Cui (Duan et al., 2018)) to replace EGFP behind IRES2 in the pIRES2-EGFP vector (Clonetech) using BstX1 and BsrG1. CRY2-iTrkA was generated from CRY2-mCherry-iTrkA (Addgene #106168; gift from Dr. Bianxiao Cui (Duan et al., 2018)) by using an adaptor with BsrG1 and Mfe1 sites to remove mCherry and then subcloned into Ctrl-Opto in front of IRES2 using Xho1 and EcoR1 sites to generate the iTrk-Opto construct. K547N-iTrk-Opto was created by PCR mutagenesis and then subcloned using the same restriction sites. iPlex-Opto and ΔKRK-iPlex-Opto was done by PCR amplification of iPlex and ΔKRK-iPlex (lacking the first KRK motif in the ICD) from full length PlexA4 (gift from Dr. Avraham Yaron (Mlechkovich et al., 2014)) and then subcloned into the iTrk-Opto construct by using BsrG1 and Mfe1 sites to replace iTrk.

For KIF1-CA-mScarlet and KIF5-CA-mScarlet, mScarlet (Addgene #85044 (Bindels et al., 2017)) was generated from PCR and subcloned into KIF1A and KIF5C-mNeonGreen (gift from Dr. Kristen Verhey (Tymanskyj et al., 2018)) using restriction sites Kpn1 and BsrG1.

shRNA constructs were generated using the oligos based on the previously validated sequences for KIF5A, B and C (Pan et al., 2019), and for KIF1A and 1B (Lipka et al., 2016). The oligos were subcloned behind the U6 promoter of a previously described vector (Tymanskyj et al., 2017), which was modified using PCR subcloning at BamH1 and BsrG1 sites to express iRFP.

DRG neuron culture

Primary rat DRG neuronal cultures were performed as described previously (Zhao et al., 2009). Briefly, DRGs were dissected out from E17 rat embryos, washed once in HBSS, and incubated at 37°C with 0.25% trypsin for 10–15 min. Trypsin-treated DRGs were resuspended in L15 medium plus 10% horse serum and then mechanically triturated with a fire-polished glass pipette. Dissociated rat DRG neurons ($\sim$7.5 × 10^5 cells) were transfected with $\sim$ 1–2 μg plasmid DNA by nucleofection (Lonza) using reagent P3 and the CU-133 program. Neurons were then plated at $\sim$30,000 cells in glass-bottom dishes coated with 10 μg/mL poly-d-lysine and 10 μg/mL laminin, and cultured in F12 medium (with N3 supplement, 40 mM glucose, and 25 ng/mL NGF) in a humidified incubator at 37°C and 5% CO_2.

Live cell imaging

After overnight culture, dishes were mounted on a heated humidified chamber (OkoLab) equilibrated to 37°C with 5% CO_2 on an inverted microscope (Zeiss Axiovert 200). Fluorescent images were acquired from live cells using a 100× apochromatic objective (NA = 1.4) on a W1 Yokogawa spinning disk system with an EMCCD camera (Cascade 512, Photometrics) using 488nm, 560nm or 640nm lasers. Based on the iRFP labeled morphology, branch junctions at axonal terminals with branches longer than 10 μm were selected for transport imaging. Images of vesicle markers were acquired every 0.5 s for 2 min. Additionally, the entire length of both axons and branches as well as the GC morphology were recorded based on iRFP, which was imaged at the beginning and the end of the 2-min imaging window.

For local activation of optogenetic experiments, the GC of a selected axon or branch expressing the optogenetic constructs was moved to a 20-μm circular spot in the center imaging field that was created by an adjustable pinhole in the light path. Activation was achieved by exposing the GC with blue light (488 nm filter) generated from a mercury lamp for 100 ms every 10 s for 2 min. Vesicle transport at the branch junction was then imaged immediately after activation (time point 0 min) and then subsequently at 7 min and 14 min (Figure 2C) using the spinning disk system described above.

For FRAP analysis, DRG neurons were transfected with mScarlet tagged KIF1-CA or KIF5-CA and imaged as described above. Photobleaching was achieved by 20–60 s exposure of green light (560nm filter) from a mercury lamp at the GC using a 50-μm circular spot, until signal was reduced or absent in the GC. Neurons were co-transfected with iRFP to monitor any laser induced damage that may affect morphology. KIF-mScarlet Images were acquired every 30 s for 10 min after photobleaching.

Image analysis and quantification

All image analyses were conducted using ImageJ. Branch lengths of each neuron were measured using the segmented line tool. The longer of the branches was defined as the axon, and the shorter the branch. For axon/branch calibers, we measured the width (W_A and W_B) of the axon and branch segment 5–10 μm adjacent to the junction. Axon/branch angles were calculated using the angle tool

in ImageJ, measured from the common axon 10–20 μm along the axon/branch. GC status for each axon and branch was recorded as either dynamic (D) or static (S) and grouped into four groups; D/D, S/D, D/S or S/S. Under the culture condition, it was rare to have two static GCs (S/S) for both branches.

For transport quantification, a segmented line was drawn to cover the common region of the axon prior to the branch junction and continued into one of the branches. This was repeated to generate another segmented line for the second branch, using the same line segment for the common region. From the two segmented lines, Kymographs were generated using the reslice tool or the multi kymograph plugin from ImageJ. The two kymographs were aligned and the split between the common region and axon/branch was marked (e.g. dotted yellow line in Figure 1B). Ant. transport events (aT_A or aT_B) travelling through the branch junction were defined as a linear track that could be followed from the common region to one of the two branches, whilst Ret. events (rT_A or rT_B) were defined as transport events traveling from either the axon or branch into the common axon. The Ant. or Ret. transport probability ($aT_A\%$, $aT_B\%$, $rT_A\%$, or $rT_B\%$) were calculated as the percentage of the number of events (aT_A, aT_B, rT_A, or rT_B) moving into/out of axons or branches divided by the total number of transport events ($aT_{Total} = aT_A + aT_B$ or $rT_{Total} = rT_A + rT_B$) into or out of axons and branches. The Ant.:Ret. ratio (aT_A/rT_A or aT_B/rT_B) was calculated as the number of Ant. events divided by the number of Ret. events for each branch at the branch junction.

For LAMP1 velocity analysis, all Ant. tracks in both control and activated branches were measured for each time point. The run velocity was calculated using length/time measured from kymographs and the formula: speed = length/time.

For optogenetic analysis, kymographs were generated and analyzed as described above for vesicle movement through branch junctions of each neuron into control and activated branches at 4 time points (pre, 0, 7 and 14 min post activation). Changes in transport for each neuron can be seen as a connected line in the figures.

For FRAP analysis, the background signal was first subtracted from that in the bleached and unbleached regions. The background subtracted signal in the bleached region was normalized based on the signal in the unbleached region at each time point. The percentage of fluorescence recovery was then determined by calculating the ratio of fluorescence change after bleaching to the fluorescence difference before and after photobleaching using the recovery equation $(F_t - F_0)/(F_{pre}-F_0)$, where F_t is the normalized fluorescence measured at each time point, F_0 is the normalized fluorescence signal immediately after photobleaching at $t = 0$ s and F_{pre} is the normalized fluorescence intensity before photobleaching.

QUANTIFICATION AND STATISTICAL ANALYSIS

Data are presented as mean ± SEM for box and whisker plots. Statistical analysis was performed in Prism 9.0 software (GraphPad). Normality was tested for each dataset using the Kolmogorov-Smirnov test. For two sample comparison, parametric data were analyzed by t test, and non-parametric data by the Mann-Whitney test. Multiple parametric samples were compared using one-way ANOVA with the Tukeys or Dunnett post hoc, whereas multiple non-parametric samples were done by the Kruskel-Wallis test with the Dunn post hoc. The statistical tests and the sample number (n) are described in the figure legends. p values smaller than 0.05 are considered significant and represented by asterisks: *$p < 0.05$; **$p < 0.01$; ***$p < 0.001$; ****$p < 0.0001$. Each experiment was carried out a minimum of three times with all the data pooled together for analysis. For each branch junction, both Ant. and Ret. transport events were counted. Since not all branch junctions had both Ant. and Ret. events, the sample number for their analysis is not always the same. However, no data points were excluded from analysis.

Because the transport outcome is binary, we used logistic regression to analyze the odds of Ant. transport into the axon as opposed to the branch (i.e., $aO = aT_A/aT_B = aT_A\%/aT_B\%$), appropriately accounting for the different number of transport events across different experiments. When evaluating the association of the transport outcome with the axon-to-branch length ratio (L_B/L_A), the caliber ratio (W_B/W_A) or the angle ratio (Θ_B/Θ_A), we used the SOLVER tool in the Excel software and the Generalized Reduced Gradient method for regression (Figures 1D–1F and S1B). When evaluating the transport outcome with both the length ratio (L_B/L_A) and the GC motility (D vs S), we used the SAS software for regression (Figures 1H, S3A, and S3C) and estimated odds ratios based on the Generalized Estimating Equations (Table S1). In both cases, the regression lines were derived after back-transformation from the odds scale to the probability scale.